F-actin dynamics regulates mammalian organ growth and cell fate maintenance

Graphical abstract

Authors

Arianna Pocaterra, Giulia Santinon, Patrizia Romani, ..., Nils Gauthier, Kristian Franze, Sirio Dupont

Correspondence

sirio.dupont@unipd.it
(S. Dupont)
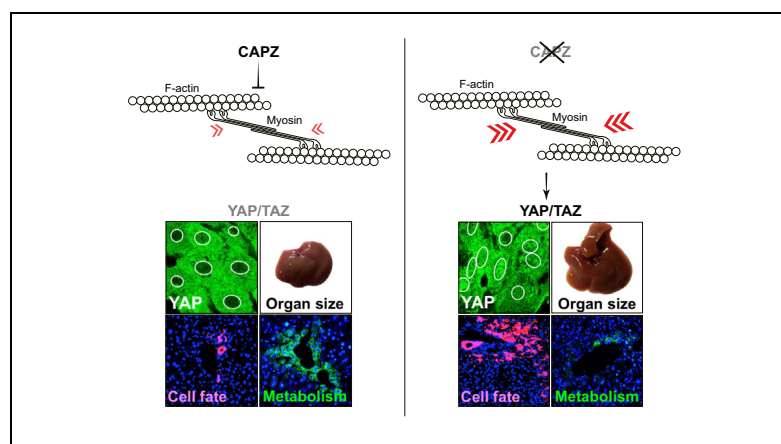
Highlights

- Absence of CAPZ leads to increased cell contractility and tissue stiffness.

- Loss of CAPZ leads to liver overgrowth, hepatocyte reprogramming and metabolic defects.

- These phenotypes are due to YAP hyperactivation, and occur in parallel to LATS1/2.

- ROCK inhibition rescues the effects of CAPZ inactivation.

- Loss of CAPZ unveils the relevance of mechanical signals for tissue homeostasis.

Lay summary

The mechanical properties of cells and tissues (*i.e.* whether they are soft or stiff) are thought to be important regulators of cell behavior. Herein, we found that inactivation of the protein CAPZ alters the mechanical properties of cells and liver tissues, leading to YAP hyperactivation. In turn, this profoundly alters liver physiology, causing organ overgrowth, defects in liver cell differentiation and metabolism. These results reveal a previously uncharacterized role for mechanical signals in the maintenance of adult liver homeostasis.

F-actin dynamics regulates mammalian organ growth and cell fate maintenance

Arianna Pocaterra[1], Giulia Santinon[1], Patrizia Romani[1], Irene Brian[1], Andrea Dimitracopoulos[2], Andrea Ghisleni[3], Alejandro Carnicer-Lombarte[2], Mattia Forcato[4], Paola Braghetta[1], Marco Montagner[1], Francesca Galuppini[5], Mariaceleste Aragona[6], Gianmaria Pennelli[5], Silvio Bicciato[4], Nils Gauthier[3], Kristian Franze[2], Sirio Dupont[1],*

[1]Department of Molecular Medicine DMM, University of Padova, Italy; [2]Department of Physiology Development and Neuroscience, University of Cambridge, UK; [3]Institute FIRC (Italian Foundation for Cancer Research) of Molecular Oncology (IFOM Institute FIRC for Molecular Oncology), Milan, Italy; [4]Department of Life Sciences, University of Modena and Reggio Emilia, Italy; [5]Department of Medicine DIMED, University of Padova, Italy; [6]ULB Université Libre de Bruxelles, Belgium

See Editorial, pages 12–13

Background & Aims: *In vitro*, cell function can be potently regulated by the mechanical properties of cells and of their microenvironment. Cells measure these features by developing forces via their actomyosin cytoskeleton, and respond accordingly by regulating intracellular pathways, including the transcriptional coactivators YAP/TAZ. Whether mechanical cues are relevant for *in vivo* regulation of adult organ homeostasis, and whether this occurs through YAP/TAZ, remains largely unaddressed.
Methods: We developed *Capzb* conditional knockout mice and obtained primary fibroblasts to characterize the role of CAPZ *in vitro*. *In vivo* functional analyses were carried out by inducing *Capzb* inactivation in adult hepatocytes, manipulating YAP/Hippo activity by hydrodynamic tail vein injections, and treating mice with the ROCK inhibitor, fasudil.
Results: We found that the F-actin capping protein CAPZ restrains actomyosin contractility: *Capzb* inactivation alters stress fiber and focal adhesion dynamics leading to enhanced myosin activity, increased traction forces, and increased liver stiffness. *In vitro*, this rescues YAP from inhibition by a small cellular geometry; *in vivo*, it induces YAP activation in parallel to the Hippo pathway, causing extensive hepatocyte proliferation and leading to striking organ overgrowth. Moreover, *Capzb* is required for the maintenance of the differentiated hepatocyte state, for metabolic zonation, and for gluconeogenesis. In keeping with changes in tissue mechanics, inhibition of the contractility regulator ROCK, or deletion of the *Yap1* mechanotransducer, reverse the phenotypes emerging in *Capzb*-null livers.
Conclusions: These results indicate a previously unsuspected role for CAPZ in tuning the mechanical properties of cells and tissues, which is required in hepatocytes for the maintenance of the differentiated state and to regulate organ size. More generally, it indicates for the first time that mechanotransduction has a physiological role in maintaining liver homeostasis in mammals.
Lay summary: The mechanical properties of cells and tissues (*i.e.* whether they are soft or stiff) are thought to be important regulators of cell behavior. Herein, we found that inactivation of the protein CAPZ alters the mechanical properties of cells and liver tissues, leading to YAP hyperactivation. In turn, this profoundly alters liver physiology, causing organ overgrowth, defects in liver cell differentiation and metabolism. These results reveal a previously uncharacterized role for mechanical signals in the maintenance of adult liver homeostasis.

Introduction

Cell behavior is powerfully regulated by the mechanical properties of the microenvironment. For example, seminal studies indicated that extracellular matrix (ECM) stiffness and the resulting cell geometry can drive the choice between proliferation, cell death or differentiation, often dominating soluble cues and oncogenes.[1–7] The current model explaining these observations is that cells probe the physical properties of the microenvironment by exerting contractile forces on adhesion complexes generated by their actomyosin cytoskeleton.[8–12] In turn, actomyosin contractility regulates intracellular signaling pathways to regulate cell behavior.

Several biochemical pathways respond to mechanical cues. Among them, Yes-associated protein 1 (YAP) and transcriptional coactivator with PDZ-binding motif (TAZ or WWTR1) are required mediators of multiple biological responses dictated *in vitro* by mechanical cues and actomyosin contractility.[13–15] YAP/TAZ function as transcriptional coactivators together with the TEAD family of transcription factors, and their activity is regulated by upstream inputs including the Hippo cascade, centered on the LATS1/2 kinases.[16,17] *In vivo*, the function of YAP and of YAP-regulatory inputs has been studied with great detail in the liver tissue, where YAP activation leads to hallmark phenotypes.[18–29]

ELSEVIER

EASL
The Home of Hepatology

Despite the increasing array of techniques to measure the mechanical properties of cells and tissues,[30] a question that remains largely unanswered is whether mechanotransduction and the control of F-actin dynamics is really at work in controlling adult tissue and organ homeostasis, and whether it does so through YAP or other pathways. Available functional data suggest a role for CAPZ as a negative regulator of YAP activity, and as one factor capable of regulating the response of mammary epithelial cells to ECM stiffness *in vitro*.[32,41,42] Yet, how regulation of actin assembly dynamics at the filament barbed end by CAPZ[31] is sufficient to trigger those phenotypes remains unknown. By genetic inactivation in mice, we identified an unexpected role for CAPZ in regulating cell contractility and tissue stiffness. This is relevant in adult hepatocytes to restrain YAP activity, such that CAPZ inactivation in the liver leads to organ overgrowth, hepatocyte dedifferentiation and alteration of physiological liver metabolic functions. These phenotypes can be rescued by inhibition of cell contractility and by inactivation of YAP, thus unveiling a role for mechanotransduction in regulating organ size and tissue homeostasis.

Materials and methods

Mice and treatments

Capzb[tm1a(EUCOMM)Wtsi] EM:04820 (EUCOMM/EMMA repository) mice were maintained in the C57BL/6 N strain. *Yap1*^{fl/fl} and *ROSA26-LSL-LacZ* mice were kindly provided by Dr. Pan. Mice were kept in standard cages with a limit of 5 mice per cage, with *ad libitum* feeding at an average temperature of 19–24 °C. Gender was random. Animal experiments were performed according to our institutional guidelines as approved by the University Animal Welfare Commission (OPBA) and authorized by the Ministry of Health (945/2015-PR and 54/2015-PR). Reporting was according to the ARRIVE guidelines.

The *neo* and *lacZ* cassettes in the targeted allele (Fig. S1A) were removed by crossing with the *CMV-FLP* deleter line, generating *Capzb*^{fl/fl} mice. Subsequent crossings were performed to obtain *Albumin-CRE-ERT2; Capzb*^{fl/fl}; *ROSA26-LSL-lacZ* mice (hereafter *Capz* LKO). Mice received 5 consecutive daily i.p. injections of tamoxifen starting at 4–6 weeks of age and were analyzed after 1 month. Control mice were mice of the same genotype but injected with corn oil only, or age-matched littermates without the *CRE* transgene and induced with tamoxifen. Crossing with the *CAGG-CRE* deleter was used to obtain *Capzb*^{+/-} mice, which were born at the expected mendelian ratio. Crossing of *Capzb*^{+/-} mice did not produce any viable *Capzb*^{-/-} offspring (not shown, but significant by chi-square test). Mice with liver specific knockout (LKO) of *Yap1* were *Albumin-CRE-ERT2; Yap1*^{fl/fl}; *Wwtr1*^{fl/fl}; *ROSA26-LSL-lacZ* (hereafter *Yap1* LKO).

For genotyping, mice were anesthetized using isoflurane to surgically remove the tail tip. Genomic DNA was extracted with NaOH at 95 °C for 30 min, followed by Tris-base pH = 8 neutralization. DNA was diluted in water and used for PCR with the following pairs of oligos: *Capzb-floxed*: CAP 71+84; *Capzb-null*: CAP 71+48; *Yap1-floxed*: P1+P2; *Yap1-null*: P1+P3. Primer sequences are provided in the CTAT table.

Mice were injected intraperitoneally with 350 mg/kg acetaminophen (APAP, #A7085 Sigma-Aldrich) in sterile 1×PBS. Serum was collected 8 h after APAP injection and livers after 24 h. Fasudil (LC-laboratories F-4660) was provided in drinking water at an estimated dose of 250 mg/kg for 2 weeks, starting at the same time as the first tamoxifen injection.

Hydrodynamic tail vein DNA injection

A total of 50 μg of PiggyBac (PB)-transposon plasmid DNA together with 10 μg of PB transposase were diluted in sterile Ringer's solution in a volume corresponding to 10% of body weight, before being injected into 4/6-week-old mice (18–22 g) via the tail vein over a maximum period of 8–10 s. PB-CAS9 and the single guide RNA PB-RFP-LATS1/2 were introduced as in Ref.[32]

Liver sampling

Trans-cardiac perfusion (29-gauge needle) with cold 1×PBS (10–20 ml) was performed on euthanized mice to reduce blood contaminants. The liver was placed in 1xPBS on ice, dissected and snap-frozen in liquid nitrogen to extract mRNA/proteins, or embedded in optimal cutting temperature compound (OCT) and stored at −80°.

Serum measurements

Alanine aminotransferase (ALT) activity was measured in serum using ALT Activity Assay (MAK052 Sigma). Mice were anesthetized with tribromoethyl alcohol (T48402 Sigma) and 2-methyl-2-butanol (240486 Sigma), and blood was collected from the retro-orbital sinus. Blood was clotted at room temperature (RT) for 1 h and centrifuged for 10 min. The serum was stored at −80° for later analysis. Blood glucose levels were measured with CountourXT glucometer (Bayer). Intraperitoneal glucose tolerance test assays were carried out by intraperitoneal injection of 2 mg/g glucose after overnight starvation.

Antibodies, western blotting and staining

Antibodies are provided in the CTAT table for immunofluorescence on liver sections, OCT-embedded tissue was cut into 5–8 μm thick sections with a Leica CM1950 cryostat. Sections were dried at RT for 30 min on a glass coverslip (VWR), and either stored dried at −80 °C or directly processed by rehydration in 1×PBS followed by fixation in 4% PFA for 15 min. Permeabilization was performed in 1xPBS-Triton 1% for 20 min. Blocking was done with 10% goat serum in 1xPBS-Triton 0.5% for 1 h at RT. Cytokeratin 19 (CK19 or KRT19)-positive area was quantified by measuring the proportion of CK19-positive pixels over the total number of pixels, by using binary thresholded pictures (ImageJ). For phalloidin staining, Alexa Fluor-conjugated phalloidin (Thermofisher) was incubated with secondary antibody in blocking buffer. For histological analysis, paraffin-embedded liver tissue was cut into 5 μm sections and stained with hematoxylin-eosin for histologic examination or with Picrosirius Red to visualize fibrosis (commercial kits and protocols). For EdU labelling, mice were injected with 12.5 mg/kg of EdU in sterile 1xPBS (A10044 Molecular Probes) 15 h before tissue sampling. Cells were incubated for 1 h with EdU prior to fixation. Liver slice or cells were fixed in PFA 4% and blocked/permeabilized for 30 min in 1×PBS 3% BSA + 0.2% Triton (1% Triton for liver slices). EdU reaction mix (100 mM Tris pH 8.5, 4 mM CuSO4, 625 nM Alexa Azide, 100 mM Ascorbic acid) was incubated for 30 min, and staining with other antibodies or DAPI was then performed as described above. Terminal deoxynucleotidyl transferase dUTP nick end labeling (TUNEL) staining was performed according to the DeadEnd™ Fluorometric TUNEL System (Promega). Images were acquired with a Leica SP5 or with a ZEISS LSM700 confocal microscope equipped with charge coupled device (CCD) camera, using Leica LAS AF or ZEN 2 software, or with a standard Leica DM5000B

microscope. Immunofluorescence on cells and western blotting was as in.[33]

RNA extraction and gene expression studies

Total liver RNA extractions were performed using Trizol (Thermo) extraction, starting from 5–10 mg of liver tissue. Contaminant DNA was removed by RNase free-DNase (Thermo). For cells, total RNA extraction was performed using RNeasy kit (Qiagen) and contaminant DNA was removed by RNase-Free DNase Set (Qiagen). RNA sequencing was carried out at the CRIBI facility of the University of Padova. Library preparation was performed using TruSeq Stranded mRNA Library Prep Kit (Illumina) according to the manufacturer's protocol, and sequenced with an Illumina NextSeq 500 platform (75 bp, SE, $\geq 15 \times 10^6$ reads/sample). Raw reads were aligned using STAR (version 2.5.3a)[34] to build version mm10 of the mouse genome. Counts for UCSC annotated genes were calculated from the aligned reads using featureCounts function of the Rsubread R package[35] in R-3.3.1. Normalization and differential analysis were carried out using edgeR R package.[36] Raw counts were normalized to obtain count per million mapped reads (CPM) and reads per kilobase per million mapped reads (RPKM). Only genes with a CPM greater than 1 in at least 4 samples were retained for differential analysis.

Retro-transcription was carried out with dT-primed M-MLV reverse transcriptase (Thermo). qPCR analyses were carried out with triplicates of each sample cDNA on QuantStudio 6 Flex Real-Time PCR System (Thermo) with a FastStart SYBR Green Master Mix (Roche). Expression levels were calculated relative to *GAPDH* based on the efficiency$^{-\Delta Ct}$ method. qPCR primer sequences are provided in the CTAT table.

Cell lines

Primary mouse adult fibroblasts (MAFs) were obtained by standard procedures after enzymatic digestion of the tail tip and plated in DMEM + 20% FBS, 1% Gln, Pen/Strep. MAFs were kept in a low-oxygen (5%) incubator to prevent stress-induced senescence. Subsequent manipulations and experiments were performed in a standard incubator. Cells were routinely tested for mycoplasma contamination (ATCC Kit). Plasmid DNA (GFP-actin, mCherry-vinculin) was electroporated according to the manufacturer's instructions. Viral infections (Adeno-empty UIowa-272 and Adeno-CRE UIowa-5) were carried out following standard procedures and protocols.

Microfabrications

Substrates were made of polyacrylamide (PAA), polymerized on standard 25 mm glass coverslips. (3-Aminopropyl) trimethoxysilane was applied to the glass surface for 3 min, followed by washes with ddH2O, and treatment with 0.5% glutaraldehyde for 30 min. A pre-mixed solution was made of 500 µl 40% acrylamide, 65 µl 100% hydroxy-acrylamide and 250 µl 2% bis-acrylamide (Bis-AA, Fisher scientific), and diluted in PBS to obtain the desired stiffness. After 15 min de-gassing, tetramethylethylenediamine and ammonium persulfate were added to initiate the cross-linking, and 50 µl of the solution was immediately pipetted onto the coverslips. A plasma-cleaned coverslip made hydrophobic with RainX (Kraco Car Care International Ltd.) was lowered onto the drop to ensure even thickness; this was later covered with PBS and removed. The gels were washed in PBS and sterilized under UV light. Gels were treated with 100 µg/ml poly-D-lysine overnight, and then with fibronectin for 1 h to promote cell adhesion. All chemicals were from Sigma-Aldrich, unless otherwise stated. Micropatterned glass slides[13] were from Cytoo SA (PADO-1 custom mask, available to all users upon request). For each slide, 80,000 cells were plated in a 6-well plate dish containing a single slide, and non-adherent cells were washed with medium after 2 h.

Fluorescence recovery after photobleaching

MAFs were re-seeded on glass-bottom dishes (Matek, Sigma-Aldrich) coated with 10 µg/ml of fibronectin 24 h after transfection (mCherry-vinculin or GFP-actin), and imaged in Ringer's phenol-red free medium upon complete spreading with a Confocal Spinning Disk microscope (Olympus) equipped with a 100×/1.35Sil silicone oil immersion objective, a iXon897 Ultra camera (ANDOR) and a fluorescence recovery after photo-bleaching (FRAP) module equipped with a 405 nm laser. Environmental control was maintained with an OKOlab incubator. Circular regions of interest (ROI) of 2 µm diameter were photo-bleached at 50% intensity for actin and 100% intensity for vinculin, and post-bleaching images were followed with 15 to 20% laser intensity for 100 frames (1 frame every second for actin, 1 frame every 0.5 seconds for vinculin). FRAP data were analyzed as reported[37] and curves fitted to a monoexponential recovery equation by the Graphpad Prism software: $I = I_0 + Imax * [1 - e^{-(k)*(t)}]$. Where I is the relative intensity compared to the pre-bleaching value, k represents the association rate constant, and t is expressed in seconds.

Total internal reflection fluorescence microscopy

Total internal reflection fluorescence (TIRF) microscopy of MAFs was performed using a DMI6000B equipped with AM TIRF module (Leica). Images were acquired using either a PlanApoN 60x1.45-NA or UApoN 100x1.49-NA TIRF oil-immersion objective, captured using an Ixon+ electron multiplying CCD (EMCCD) camera (Andor). All images were acquired with the same camera settings and laser intensity for consistent image analysis. A custom macro, available upon request, was designed to quantify the number and size of focal adhesions per cell. Images containing a single cell were background-subtracted and a binary mask was created by applying non-linear filters. The mask was then applied on raw images to obtain particle sizes and area. Only particle sizes >200 nm^2 were considered in the analysis, as this avoided analysis of background particles. All images were acquired with the same settings and consistently analyzed by concatenating all images, while saturated images were discarded.

Traction force microscopy

Preparation of PAA substrates. PAA gels were prepared on imaging dishes (µ-Dish, Ibidi, Germany) as previously described.[38] Fluorescent nanoparticles (FluoSpheres carboxylate, 0.2 µm, crimson, Life Technologies, UK) were added to the PAA pre-mixes, which were then placed in an ultrasonic bath for 30 s to separate the beads. After starting polymerization, the imaging dish was inverted to ensure that beads settled close to the gel surface.

Time lapse imaging for traction force microscopy (TFM). MAFs were seeded onto PAA gels with shear storage moduli G' of 1 kPa ('soft') and 10 kPa ('stiff'). After 24 h, cells where imaged using an inverted microscope (Leica DMi8) at 37 °C and 5% CO$_2$, equipped with a digital sCMOS camera (ORCA-Flash4.0, Hamamatsu Photonics), an EL6000 illuminator (Leica,

Germany), and a 63× oil objective (NA1.4, Leica, Germany). Images were acquired using Leica LAS X software. Fluorescence images of beads, and widefield images of cells were taken every 2 min. After image acquisition, culture media were exchanged with Trypsin-EDTA (Gibco) to detach cells from the gel. Reference images of fluorescent beads were taken 15 min after trypsinization. Three independent traction force experiments were performed for each condition.

Data analysis for TFM. Traction stress maps were calculated for each frame using a TFM Software Package in ImageJ.[39] To minimize noise, regularization parameters of 0.01 and 0.00001 were chosen for cells on 1 kPa and 10 kPa PAA gels, respectively. Traction stresses were averaged over time for each cell. Post-processing of the data and statistical analyses were done with a custom Python script. The distributions of the average stresses were compared using Mann-Whitney U tests.

Atomic force microscopy

All atomic force microscopy (AFM) experiments were performed in accordance with the UK Animals (Scientific
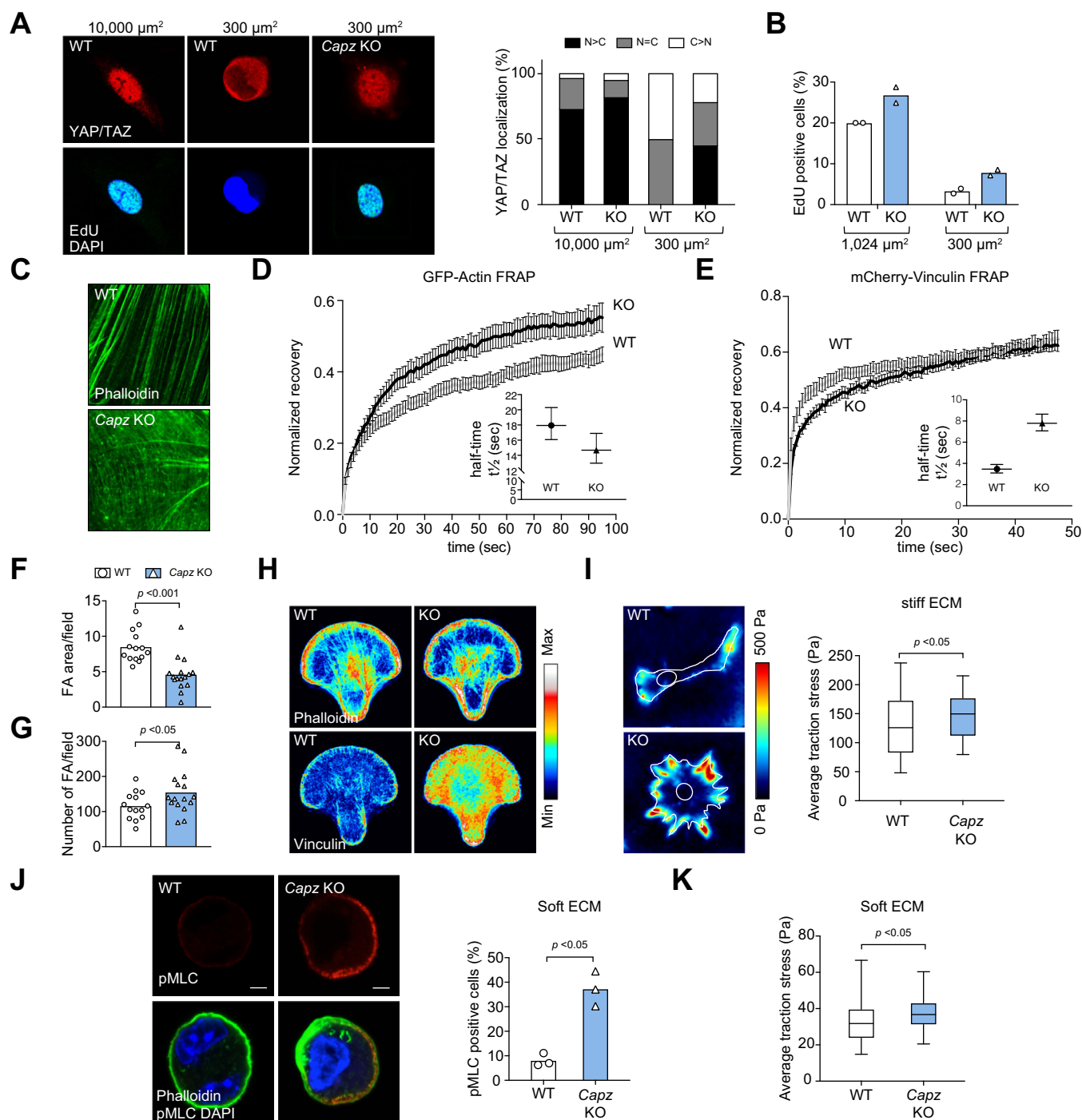
Procedures) Act 1986. Mice were sacrificed via an approved schedule 1 method. Livers were immediately dissected and embedded in low melting point agarose (4% in PBS; Sigma-Aldrich). A small block of agarose containing the sample was submerged in chilled PBS and cut into 500 μm thick sections using a vibratome (Leica). Sections were slowly heated to 37 °C in PBS for 30 min prior to AFM measurements. AFM measurements were carried out similarly to the method previously described.[40] Monodisperse polystyrene beads (radius r = 18.64 μm ± 0.17 μm, microParticles GmbH, Berlin, Germany) were glued to tipless silicon cantilevers (spring constants between 0.01 and 0.03 N/m; Arrow-TL1, NanoWorld, Neuchatel, Switzerland). The AFM was mounted on an x/y motorized stage of an inverted microscope (AxioObserver A1, Zeiss, Cambridge, UK). Cantilever position relative to the liver sections was monitored via a CCD camera (The Imaging Source, Bremen, Germany) placed on top of the AFM setup. Force-distance curves were taken with a set force of 10 nN with an approach speed of 10 μm/s. Apparent elastic moduli K were calculated using the Hertz model: $F = 4/3\ K\ r^{1/2}\ \delta^{3/2}$ for an indentation depth δ = 2 μm, using a custom written automated algorithm based in Matlab (MathWorks, Natick, USA). Stiffness was measured in maps over defined sample areas, over which multiple force-distance curves were taken at 20 μm steps (each map containing 40–200 measurements, 2–3 maps per liver). The median measurement stiffness for each map was calculated, and statistical significance between maps was determined using a 2-tailed Student's t test.

Statistical analysis

Data analyses were performed using GraphPad Prism software. Graphs indicate mean values and single values of all biological replicates (or mice), unless otherwise indicated. Data for each mouse are derived from analysis of multiple (n ≥6) tissue sections. To facilitate gene expression data visualization, the mean expression levels in WT mice were set equal to 1, and all other data (single values, means and errors) are relative to this. Significance was calculated by applying unpaired Mann-Whitney U tests (n = 3 samples) or Student's t tests (n ≥4 samples); for RNA sequencing, we considered as significant only genes with p <0.05.

Data availability

Data that support the findings are available within the manuscript or upon reasonable request to the corresponding author. RNA seq data have been deposited in GEO database (GSE116993).

For further details regarding the materials used, please refer to the CTAT table and supplementary information.

Results

Derivation and validation of a *Capzb*-floxed allele

To functionally dissect the role of mechanotransduction and F-actin dynamics *in vivo*, we chose to inactivate the F-actin capping protein CAPZ. CAPZ is a dimer whose alpha subunit is encoded by 2 loci in mammals (*Capza1* and *Capza2*), while the beta subunit is encoded by only 1 gene (*Capzb* – Gene ID: 12345), facilitating genetic analysis. We thus recombined the *Capzb*^tm1a(EUCOMM)Wtsi allele to obtain *Capzb*^fl/fl mice (see Methods and Fig. S1A-B); the same allele was recently used in Ref.[41] We validated this allele by monitoring efficient depletion of the endogenous CAPZB protein in primary adult *Capzb*^fl/fl fibroblasts recombined by adenoviral-CRE infection (Fig. S1C). Moreover, adenoviral-CRE recombination of primary newborn *Capzb*^fl/fl cardiomyocytes led to a rapid disassembly of contractile actomyosin structures (Fig. S1D), in line with the role of CAPZ in muscle sarcomeres.[31] We speculate this defect might underlie the lethality of *Capzb*^−/− embryos (see methods).

We also aimed at specifically validating the role of CAPZ in the context of mechanotransduction. For this we compared the biological response of WT (*Capzb*^fl/fl + adeno-control) and *Capz* KO (*Capzb*^fl/fl + adeno-Cre) primary adult fibroblasts (MAFs) to mechanical cues: WT MAFs respond to a small cell geometry, which is associated with decreased actomyosin contractility,[42] by inactivating YAP/TAZ and by decreasing proliferation (Fig. 1A and B), in line with Ref.;[13,14] in contrast, *Capz* KO MAFs retained nuclear YAP and kept proliferating, at least to a certain extent (Fig. 1A and B). As a control, *Capz* KO MAFs completely detached from the substratum that maintains YAP nuclear exclusion (not shown). Thus, *Capzb* is required in MAFs for the inhibition of YAP in conditions of decreased contractility.

Fig. 1. The F-actin capping protein *Capzb* regulates cellular forces *in vitro*. (A) Representative pictures of control (WT) and *Capz* KO MAFs plated for 24 h on microprinted fibronectin-coated islands of the indicated adhesive area and stained for YAP/TAZ and EdU incorporation. Quantification of nuclear YAP/TAZ on the right. n = 2 (>100 cells per condition in total). Scale bar = 10 μm. (B) Quantification of proliferation in MAFs plated as in A, as assayed by EdU incorporation. n = 2 (>100 cells per condition in total). (C) Representative high-magnification immunofluorescent staining for F-actin bundles (phalloidin) in the cytoplasm of WT and *Capzb*-null MAFs. n = 3 with consistent results. Scale bar = 3 μm. (D) and (E) fluorescence recovery after photobleaching analysis of WT and *Capzb*-null MAFs transfected with GFP-actin (D) or mCherry-vinculin (E), indicated as mean and SEM Inset: half-time (t1/2) and 95% CI of actin recovery calculated by fitting the data to a monoexponential function. See Fig. S1E-F for representative images. n = 2 (D: >25 cells per condition in total; E: >40 cells per condition in total). Scale bar = 1.5 μm. (F) and (G) Quantification of the number (F) and size (G) of FAs by total internal reflection fluorescence of MAFs transfected with mCherry-vinculin. See Fig. S1G for representative images. n = 2 (16 cells per condition). (H) Average F-actin (phalloidin) and vinculin immunofluorescence stainings in WT and *Capzb*-null MAFs plated on cross-bow fibronectin-coated micropatterns. Immunofluorescence of multiple individual cells on ECM micropatterns were stacked (n = 25 per condition); the resulting image shows the average pixel intensity as a multicolor look-up table. Scale bar = 5 μm. (I) Traction force analysis of WT and *Capzb*-null MAFs plated on stiff (G′ = 10 kPa) fibronectin-coated polyacrylamide hydrogels. n = 2 (50 cells per condition). Left: representative force maps with cell and nucleus contour overlaid. Local force is indicated by a multicolor look-up table. Right: box plot (median, quartiles and extremes). n = 3 (50 cells per condition). (J) Representative immunofluorescent stainings for pMLC and F-actin bundles (phalloidin) in WT and *Capzb*-null MAFs plated on soft (G′ = 1 kPa) hydrogels. On the right: quantification of cells displaying pMLC staining. n = 3 (80 cells per condition). Scale bar = 3 μm. (K) Traction force analysis of WT and *Capzb*-null fibroblasts plated on soft (G′ = 1 kPa) hydrogels. Box plot (median, quartiles and extremes). n = 3 (50 cells per condition). Unless otherwise indicated, graphs are average and single points with unpaired 2-tailed Student's t test. Immunostainings were repeated in independent experiments, and a representative result is shown. FAs, focal adhesions; GFP, green fluorescence protein; KO, knockout; LKO, liver specific KO; MAFs, mouse adult fibroblasts; pMLCs, phosphorylated myosin light chain; WT, wild-type.

Capzb limits actomyosin contractility in response to ECM mechanical cues

We then sought to understand at what level CAPZ acts to regulate mechanotransduction. We analyzed F-actin and focal adhesions (FAs) in WT and *Capz* KO MAFs, as these are critically involved in cell mechanics. Phalloidin staining on fixed cells indicated thinner and denser bundles in *Capz* KO MAFs (Fig. 1C). FRAP analysis of actin dynamics in stress fibers indicated a faster recovery in *Capz* KO cells (Fig. 1D and Fig. S1E), and thus a faster actin turnover previously associated with higher levels of Myosin-II activity.[43,44] Analysis of vinculin dynamics in FAs indicated a slower recovery in *Capz* KO cells (Fig. 1E and Fig. S1F), and thus more stable vinculin, a typical feature observed upon increased pulling forces or upon stiffening of the ECM.[45–48] This was associated with a higher number of vinculin-positive FAs, but of smaller size (Fig. 1F-G and Fig. S1G). During these analyses we noted a redistribution of FAs from a predominantly peripheral to a more central position, perhaps reminiscent of the recently described perinuclear FAs which were specifically associated with increased tension and YAP activity;[49] to quantify this phenotype we plated MAFs on cross-bow shaped fibronectin micropatterns and averaged the intensity of the staining over several stacked cells,[50,51] confirming our observation (Fig. 1H). Furthermore, *Capz* KO MAFs dis-
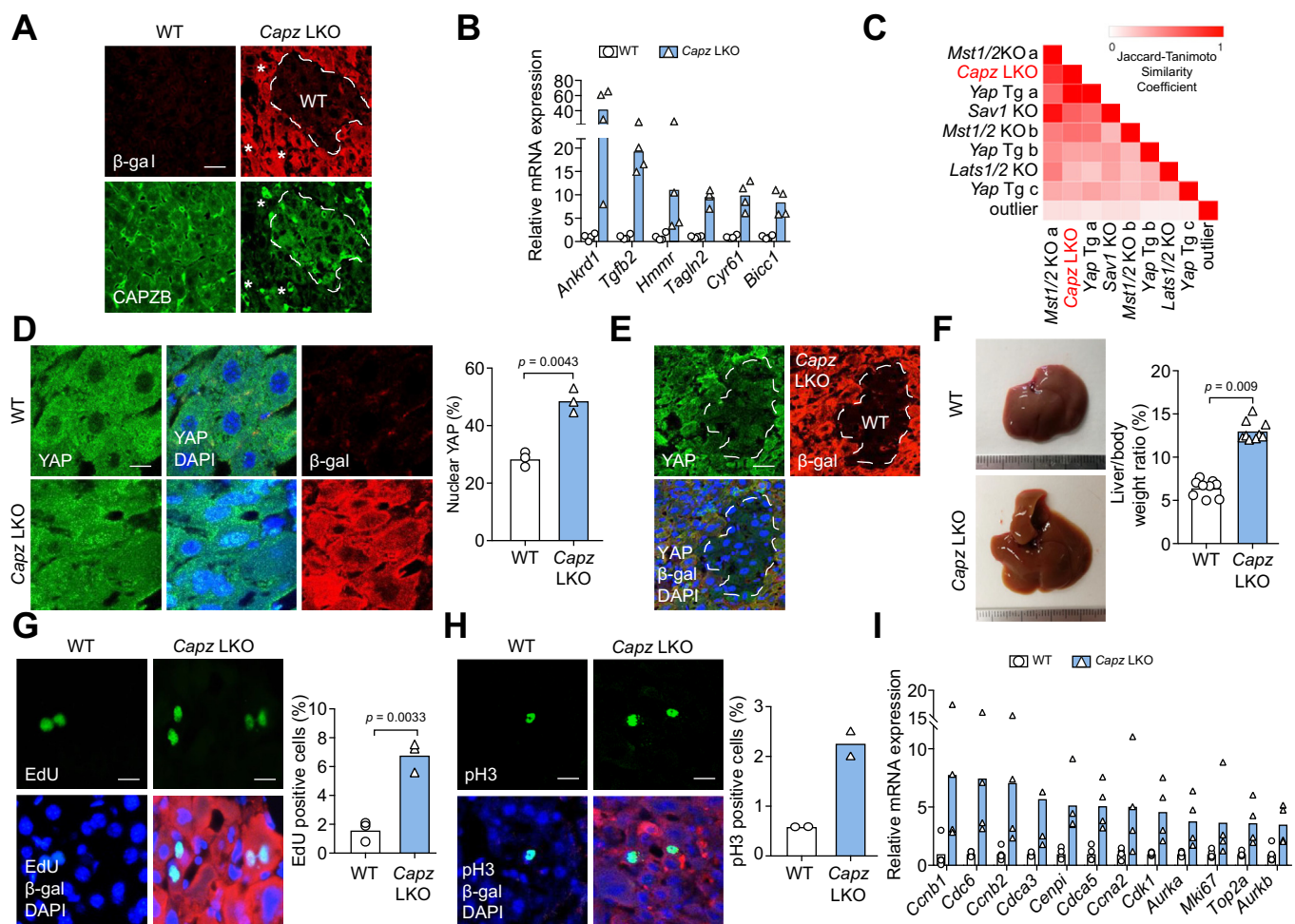
Fig. 2. *Capzb* restricts YAP activity, prevents liver overgrowth and maintains adult hepatocyte quiescence. (A) Immunostaining for endogenous CAPZB in liver sections from control (WT) and *Capz* LKO mice. Asterisks indicate non-hepatocyte cells that remain positive for CAPZB. Occasional patches of non-recombined cells (WT, white dotted line) surrounded by the *Capzb*-null tissue (positive for β-galactosidase) serve as internal control. Scale bar = 20 μm. (B) Expression of established YAP/TAZ target genes, as measured by RNA sequencing of whole livers from control and *Capz* LKO mice. Average expression levels in control (WT) mice were arbitrarily set equal to 1, and all other data are relative to this. n = 4 for each genotype. (C) Similarity matrix between *Capz LKO*, *Hippo* LKO (Mst1/2 a[78] b[28], Sav1/WW45[78], Lats1/2[26]), *Yap1* liver transgenics (Tg a[60] b[18] c[20]), and an unrelated LKO (outlier[79]). Coefficients were calculated for the indicated pairwise comparisons based on genes significantly overexpressed (fold >1.5; *p* ≤0.05). (D) Left: representative Immunostaining for YAP in liver sections from control (WT) or *Capz* LKO mice. DAPI serves as nuclear counterstain. Scale bar = 10 μm. Right: quantification of hepatocytes displaying nuclear YAP. n = 3 for each genotype. (E) Low magnification YAP immunofluorescence in a liver section from a *Capz* LKO mouse with occasional non-recombined hepatocytes (WT). n = 3 mice were consistent. Scale bar = 20 μm. (F) Representative pictures of control (WT) and *Capz* LKO livers upon dissection. On the right: quantification of body/liver weight ratio (see also Table S1). n = 9 for each genotype. (G) and (H) Representative stainings for EdU (G, n = 3 for each genotype) and phospho-Histone3 (H, n = 2 for each genotype) and their quantifications. Scale bars = 10 μm. (I) Expression of proliferation marker genes as measured by RNA sequencing of whole livers from control and *Capz* LKO mice. Average expression levels in control (WT) mice were arbitrarily set equal to 1, and all other data are relative to this. n = 4 for each genotype. Graphs are average and single points (mice) with unpaired 2-tailed Student's *t* test with Welch's correction. Immunostainings were repeated in independent sections of independent mice (see methods), and a representative result is shown. KO, knockout; LKO, liver specific KO; WT, wild-type.

play increased levels of active S19-phosphorylated myosin light chain (pMLC – Fig. S1H) and increased cellular forces on stiff hydrogels ($G' = 10$ kPa), as measured by traction force microscopy (Fig. 1I). Finally, we extended these findings in the context of a soft ECM microenvironment, where CAPZ inactivation is relevant to regulate YAP/TAZ:[52] pMLC staining was almost undetectable in MAFs on soft hydrogels ($G' = 1$ kPa), but clearly visible in *Capz* KO MAFs (Fig. 1J). Moreover, *Capz* KO MAFs exerted significantly higher forces on their substratum in this condition compared to control cells (Fig. 1K). Collectively, these data indicate that deletion of *Capzb* enables the development of higher cellular forces even in conditions of decreased extracellular resistance, unveiling a previously unsuspected role for CAPZ. Moreover, this validates *Capz* inactivation as a meaningful tool to modulate F-actin dynamics and cell mechanics *in vivo*.

Conditional inactivation of *Capzb* in hepatocytes activates the YAP mechanotransducer

To probe the role of *Capzb* as a regulator of tissue physiology we focused on the liver, because hepatocytes are inherently mechanosensitive[1,53] and because it is a model system for Hippo/YAP.[54–56] We thus obtained *Capz* LKO, wherein *Capzb* was deleted in adult hepatocytes in a time-controlled manner, enabling the lineage tracing of recombined cells by β-galactosidase expression (Fig. 2A, Fig. S2A and B).

We initially sought to find evidence for activation of the YAP mechanotransducer in *Capz* LKOs. We monitored a series of established YAP target genes in the liver tissue,[18,26] and found them upregulated in *Capzb*-null livers (Fig. 2B). Similarly, we performed a more global analysis of gene expression and found that genes activated in *Capz* LKOs are remarkably overlapping
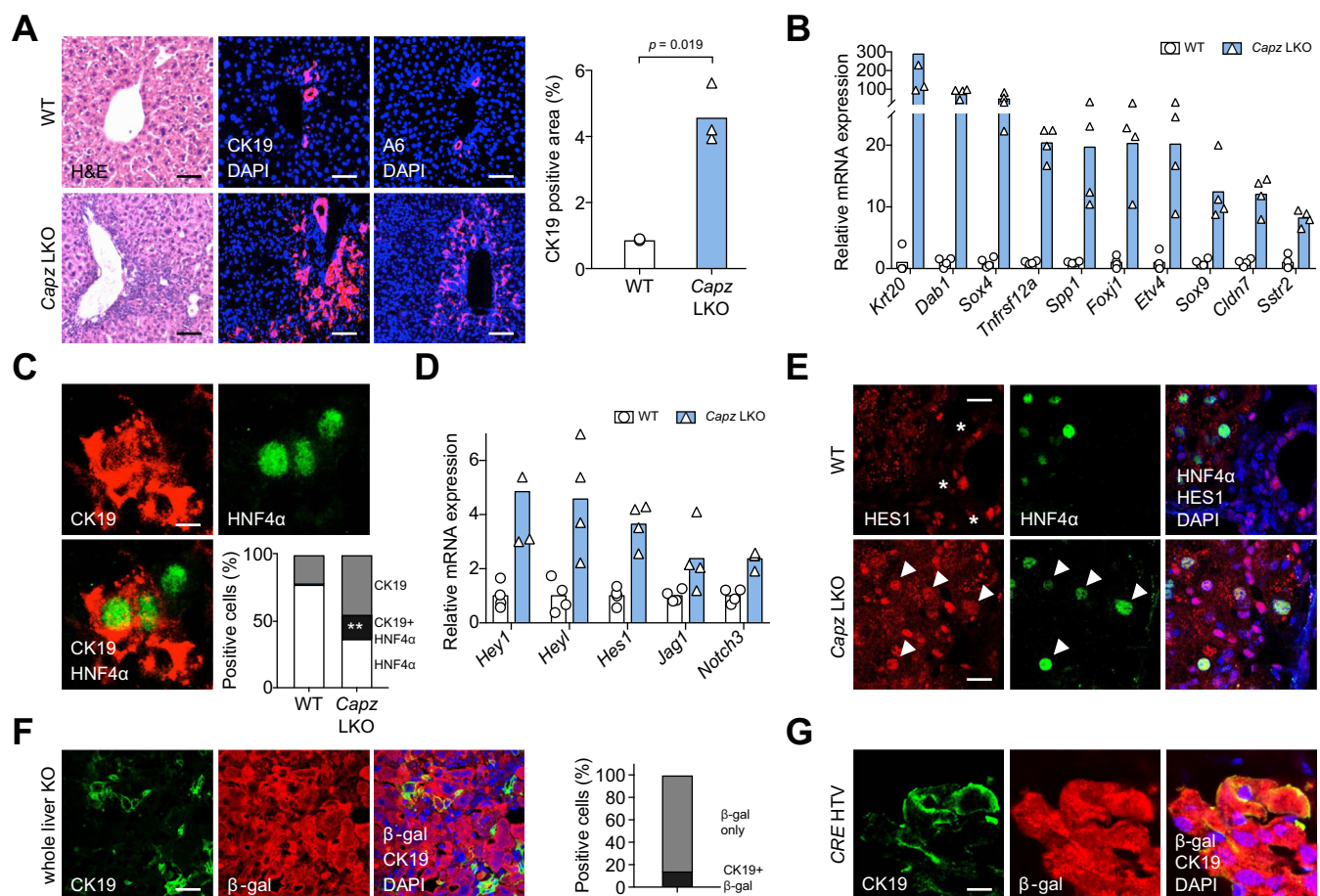
Fig. 3. *Capzb* is required to maintain hepatocyte cell differentiation. (A) Representative (H&E, left) and immunostainings for the atypical ductal cell markers CK19 and A6 (center and right) in control (WT) and *Capz* LKO liver sections. Quantification of the CK19-positive area in sections containing the portal area. n = 3 per genotype. Scale bar = 100 μm. (B) Expression of liver progenitor/cholangiocyte markers as measured by RNA sequencing of whole livers from control and *Capz* LKO mice. Average expression levels in control (WT) mice were arbitrarily set equal to 1, and all other data are relative to this. n = 4 for each genotype. (C) Appearance of cells double-positive for differentiated hepatocyte (HNF4α) and atypical ductal cell (CK19) markers in *Capz* LKO livers. Scale bar = 5 μm. Quantification in sections of the portal area. n = 3 for each genotype. **p <0.01. (D) Expression of Notch pathway and Notch target genes as measured by RNA sequencing of whole livers from control and *Capz* LKO mice. Average expression levels in control (WT) mice were arbitrarily set equal to 1, and all other data are relative to this. n = 4 for each genotype. (E) Representative immunostainings for HES1 in control (WT) and *Capz* LKO liver sections. HES1 is restricted to bile duct cells (asterisks) in WT mice. Co-localization with HNF4α (arrowheads) was only observed in *Capz* LKO mice. Scale bar = 15 μm. (F) Double immunofluorescence for CK19 and β-galactosidase (used as hepatocyte lineage tracer) in *Capz* LKO livers (*whole liver* KO). Quantification in sections not containing the portal area. Scale bar = 30 μm. (G) Double immunofluorescence for CK19 and β-galactosidase (used as hepatocyte lineage tracer) in *Capzb*^fl/fl; *ROSA26-LSL-lacZ* mice with live hydrodynamic tail vein injection of Cre-transposon plasmid, inducing recombination in single hepatocytes. Scale bar = 15 μm. Graphs are average and single points (mice) with unpaired 2-tailed Student's *t* test with Welch's correction. Immunostainings were repeated in independent sections of independent mice (see methods), and a representative result is shown. H&E, hematoxylin and eosin; KO, knockout; LKO, liver specific KO; WT, wild-type.

with those activated in *Hippo*-mutants[26,28,57] and *Yap1*-transgenics[18,20,58] (Fig. 2C). Prompted by these results, we directly monitored endogenous YAP localization by immunofluorescence, and found increased nuclear localization in *Capzb*-null hepatocytes (Fig. 2D and Fig. S2H). Of note, mutant liver tissues also display an overall increase in YAP staining intensity (Fig. 2E).

Control of liver organ size by inactivation of *Capzb*

Phenotypically, inactivation of *Capzb* caused an evident hepatomegaly reaching on average 200% of the normal liver/body weight ratio (Fig. 2F). Hepatocytes appeared enlarged, similarly observations in *Lats1/2* knockouts[26] (see Fig. S2A), and exhibited a stark increase in proliferation as measured by EdU incorporation (*i.e.* S-phase) and phospho-Histone3 (*i.e.* mitosis) staining (Fig. 2G and H and Fig. S2C). This was accompanied by overexpression of several proliferation markers (Fig. 2I), including known direct YAP targets,[58,59] and of antiapoptotic genes (Fig. S2D). As a control, we excluded major alterations of cell-cell junctions (Fig. S2E), previously observed by *Capz* inactivation in flies,[60] fibrosis (see Fig. S2A) and inflammation (Fig. S2F and G). This indicated that CAPZ is required in adult hepatocytes to keep control over a key mechanotransduction pathway, and that it potently restrains hepatocyte proliferation.

Capzb controls liver cell fate

Activation of YAP in hepatocytes leads to expansion of atypical ductal cells (ADCs)/oval cells/biliary epithelial cells that display bipotent progenitor identity.[20,23] Analysis of *Capz* LKO livers indicated a massive expansion of A6- and CK19-positive ADCs forming disorganized strands in the liver parenchyma, mainly distributed around the portal area (Fig. 3A), and this was accompanied by increased expression of cholangiocyte/progenitor markers[20,61] in *Capz* LKO livers (Fig. 3B). Appearance of ADCs upon YAP activation has been attributed to dedifferentiation of hepatocytes, with appearance of cells double-positive for CK19 and HNF4α (markers for the cholangiocyte and hepatocyte lineages, respectively),[20] which we also found in *Capz* LKO livers (Fig. 3C). Moreover, in keeping with a role for Notch in regulating hepatocyte dedifferentiation,[20,62] we found the Notch pathway activated in *Capz* LKO livers (Fig. 3D and E). To unequivocally trace ADCs to hepatocytes bearing *Capzb* deletion, we performed a double staining for β-galactosidase (which labels recombined hepatocytes) and CK19, and found co-localization (Fig. 3F). Of note, this indicated dedifferentiation of hepatocytes also at a distance from the portal area. As an alternative approach, we expressed a *Cre* transgene in hepatocytes of *Capzb*^{fl/fl} mice by hydrodynamic tail vein transposon DNA injection,[63] which caused appearance of cells doubly positive for CK19 and β-galactosidase (Fig. 3G). This indicates a cell-autonomous function of *Capzb*. More generally, these data indicate that *Capzb* inactivation is sufficient to reprogram adult hepatocyte fate.

Capzb controls hepatocyte zonation and liver metabolism

Metabolism in the liver parenchyma is zonated, with hepatocytes expressing different metabolic genes along the periportal
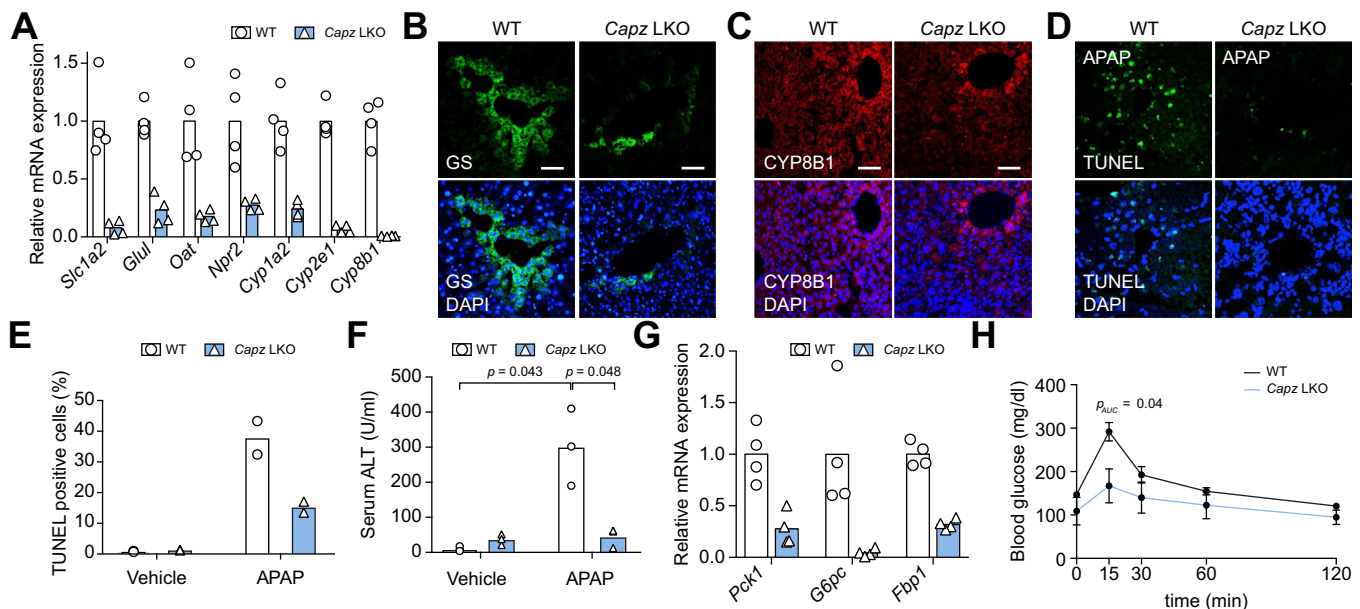
Fig. 4. *Capzb* controls hepatocyte zonation and liver metabolism. (A) Expression of pericentral hepatocyte marker genes as measured by RNA sequencing of whole livers from control and *Capz* LKO mice. Average expression levels in control (WT) mice were arbitrarily set equal to 1, and all other data are relative to this. n = 4 for each genotype. (B) and (C) Immunofluorescence for the pericentral hepatocyte markers GS (B) and CYP8B1 (C) on liver sections from control (WT) and *Capz* LKO mice, in the region of the central vein. Scale bar = 80 μm (B), 120 μm (C). (D) Analysis of cell death by TUNEL staining of pericentral liver sections in control (WT) and *Capz* LKO mice 24 h after injection with a toxic dose of APAP. Scale bar = 80 μm. (E) Quantitative analysis of TUNEL staining in control (WT) and *Capz* LKO mice 24 h after injection with a toxic dose of APAP or vehicle (control) n = 2 mice for each genotype. (F) Serum ALT levels were measured from sera of mice 8 h after APAP injection, as in (D) n = 3 mice for each genotype. (G) Expression of gluconeogenesis enzymes as measured by RNA sequencing of whole livers from control and *Capz* LKO mice. Average expression levels in control (WT) mice were arbitrarily set equal to 1, and all other data are relative to this. n = 4 for each genotype. (H) Glucose tolerance test after intraperitoneal injection in control (WT) and *Capz* LKO mice. Statistical significance was calculated on the area under the curve values. Average and SEM n ≥4 mice for each genotype. Graphs are average and single points (mice) or SEM with unpaired two-tailed Student's *t* test with Welch's correction. Immunostainings were repeated in independent sections of independent mice (see methods), and a representative result is shown. ALT, alanine aminotransferase; APAP, acetaminophen; GS, glutamine synthase; KO, knockout; LKO, liver specific KO; TUNEL, terminal deoxynucleotidyl transferase dUTP nick end labeling WT, wild-type.

to pericentral axis of the hepatic lobules in response to several signaling cues.[64–66] Recent evidence indicates that YAP activity contributes to zonation by inhibiting pericentral gene expression.[28] We thus checked for expression of established pericentral markers in *Capz* LKO livers and found them strikingly reduced both at the mRNA level (Fig. 4A) and by immunostaining (Fig. 4B and C). Pericentral zonation is particularly evident if looking at the expression of cytochromes involved in xenobiotic metabolism.[66,67] Among these we focused our attention on *Cyp1A2* and *Cyp2E1*, the main genetic determinants of APAP toxicity in the mouse,[68] which we found strongly inhibited (see Fig. 4A). Reflecting decreased expression, we then found that *Capz* LKO were extremely resistant to APAP intoxication: at sub-lethal doses (350 mg/kg) sufficient to cause extensive cell death (as measured by TUNEL assay) and extensive hepatic damage (as measured by serum ALT) in WT mice, *Capz* LKO mice remained insensitive (Fig. 4D-F).

Another recently reported function of YAP in the liver is the regulation of gluconeogenesis and blood glucose homeostasis.[29] Accordingly, we found decreased expression of key gluconeogenic genes in *Capz* LKO mice (Fig. 4G), and this was functionally linked to decreased steady-state blood glucose levels

and improved glucose tolerance (Fig. 4H). Overall, these data indicate that *Capzb* is relevant to maintain the physiological patterning of hepatocyte differentiation and of key metabolic traits in the liver.

Capzb regulates liver homeostasis through YAP

To obtain formal evidence that phenotypes observed upon *Capzb* inactivation are due to YAP activation, and not to other mechanoresponsive pathways, we deleted *Yap1*[22] in *Capz* LKOs (*Albumin-CreERT2; Capzb*^{fl/fl}*; Yap1*^{fl/fl}*; ROSA26-LSL-lacZ* mice, *Capz+Yap1* LKO). As shown in Fig. 5A-E and Fig. S3A, *Yap1* inactivation partially rescued hepatomegaly and proliferation, while it almost completely rescued atypical ductal cell expansion, pericentral expression, and glucose tolerance. We speculate the partial rescue might depend on TAZ, which is functional in hepatocytes[69] and sufficient to induce hepatocyte proliferation (see Fig. 5G). This would also imply that the phenotypes described above require different thresholds of YAP/TAZ activity. Thus, the control of F-actin assembly dynamics is a physiologically-relevant input to keep control over YAP/TAZ activity in the liver.
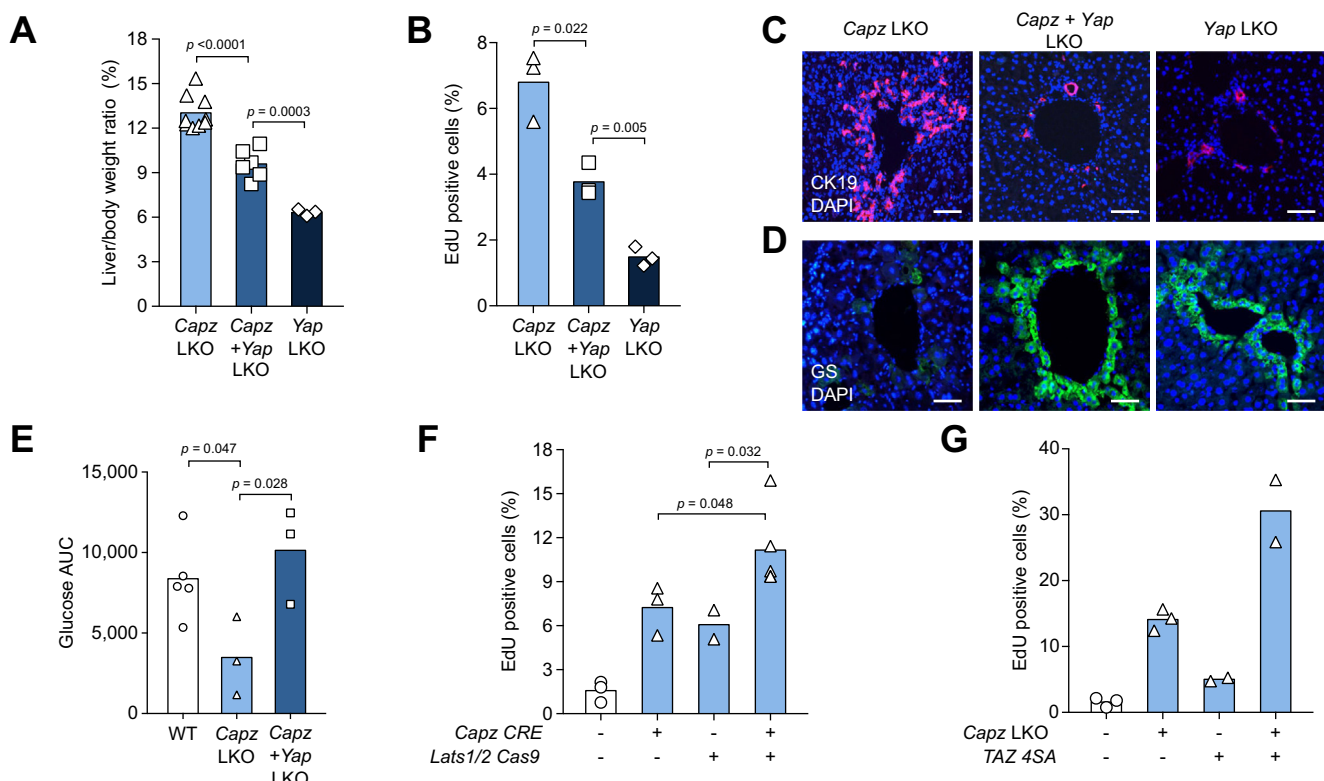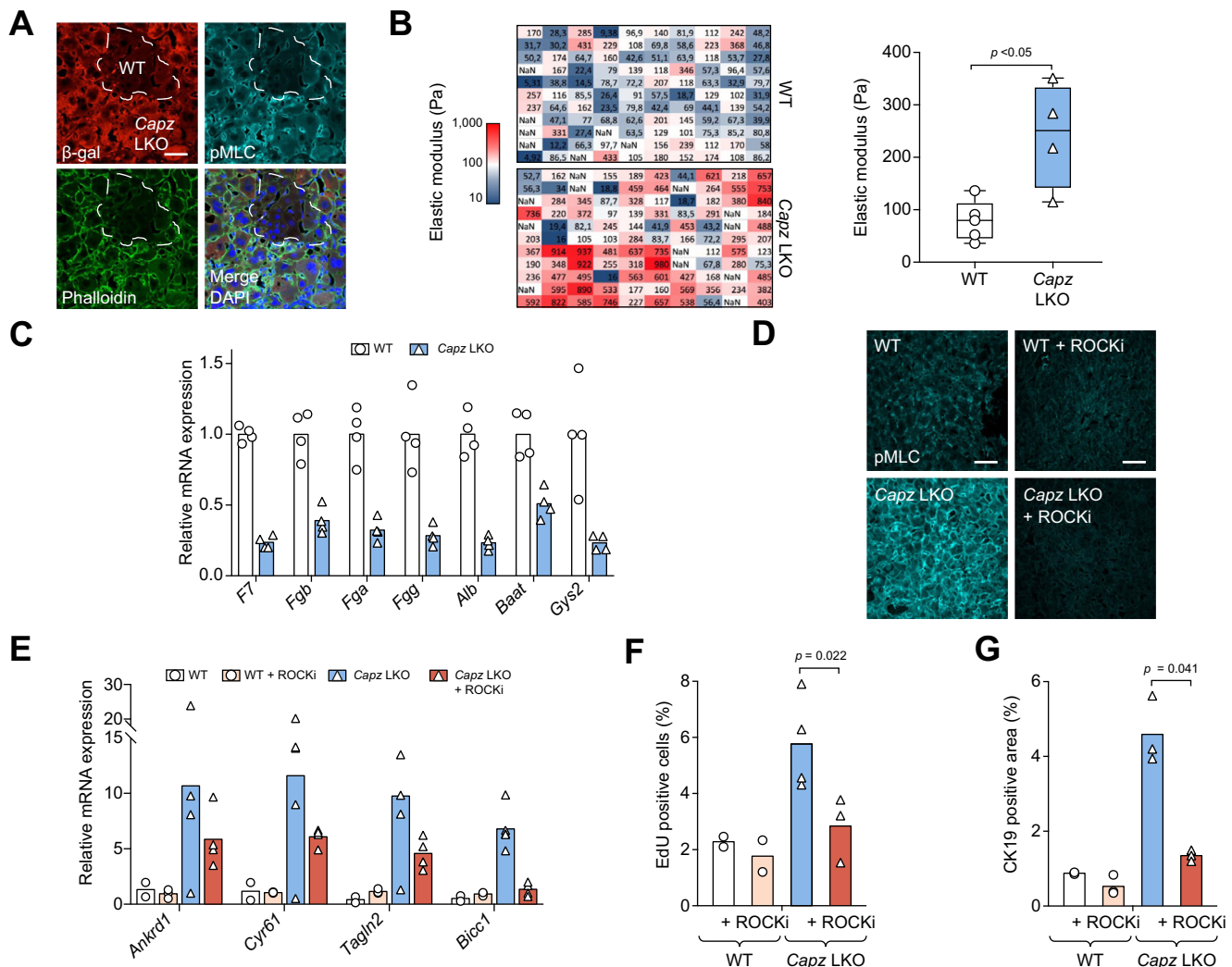

Fig. 5. *Capzb* regulates liver homeostasis through *YAP1* and in parallel to Hippo. (A) Liver/body weight ratio of the indicated *Capz* LKO, *Capz+Yap1* LKO (n >6 for each genotype) and *Yap1* LKO mice (n = 3). (B) EdU incorporation in the indicated mice. n = 3 for each genotype. (C) and (D) Representative immunofluorescence for the atypical ductal cell marker CK19 (C) and for the pericentral marker GS (D) on liver sections from the indicated mice. n = 3 mice were consistent for each staining. Scale bar = 100 μm (C), 80 μm (D). (E) Glucose tolerance test upon intraperitoneal injection as measured by glucose AUC in mice of the indicated genotypes. WT are control mice. (F) Quantification of EdU incorporation in control livers (*Capzb*^{fl/fl}*; ROSA26-LSL-lacZ* mice injected with GFP transposon), in livers with single-cell inactivation of *Capzb* (*Capz CRE*: *Capzb*^{fl/fl}*; ROSA26-LSL-lacZ* mice injected with CRE transposon), with single-cell inactivation of *Lats1/2* (*Lats1/2 CAS9*: *Capzb*^{fl/fl}*; ROSA26-LSL-lacZ* mice injected with RFP-Lats1/2-sgRNA and CAS9-expressing transposon), or their combination. Hepatocytes were transduced by hydrodynamic tail vein injection. n = 3 for each genotype. See Fig. S3E for representative stainings. (G) Quantification of EdU incorporation in control and *Capz* LKO livers injected with GFP or with TAZ-4SA transposons. Hepatocytes were transduced by hydrodynamic tail vein injection. n = 2 for each genotype. See Fig. S3F for representative stainings. Graphs are average and single points (mice) with unpaired 2-tailed Student's *t* test with Welch's correction. Immunostainings were repeated in independent sections of independent mice (see methods), and a representative result is shown. AUC, area under the curve; GFP, green fluorescence protein; GS, glutamine synthase; sgRNA, single guide RNA; KO, knockout; LKO, liver specific KO; WT, wild-type.

Capzb regulates YAP/TAZ in parallel to Hippo

Some data suggest that mechanical regulation of YAP/TAZ involve YAP phosphorylation by LATS kinases; functional data however indicate that mechanical regulation of YAP/TAZ can occur in the absence of LATS1/2.[15] The effectiveness of *Capzb* inactivation in regulating YAP/TAZ in hepatocytes offered us the opportunity to test the genetic interaction with *Lats1/2* *in vivo*. We thus expressed in the liver, by hydrodynamic tail vein transposon injection, the CAS9 enzyme and guide-RNAs targeting *Lats1* and *Lats2*,[32] to inactivate *Lats1/2* without inducing liver failure caused by whole-organ knockout.[26,70] CRISPR inactivation of *Lats1/2* induced multiple *Yap1*-dependent phenotypes (Fig. S3B-D), indicating efficient recombination of both genes.[26,32,71,72,83] We then found that the combination of *Capzb* and *Lats1/2* inactivation induced a higher number of proliferating cells compared to *Lats1/2* inactivation alone (Fig. 5F and Fig. S3E), ruling out the possibility that CAPZ works only through LATS1/2 to regulate YAP. We also injected a transposon plasmid encoding TAZ-4SA (a TAZ isoform that cannot be phosphorylated and inhibited by LATS kinases) and obtained a comparable cooperation with *Capzb* deletion (Fig. 5G and Fig. S3F). Overall this indicates that regulation of YAP/TAZ by actin

Fig. 6. *Capzb* **regulates liver homeostasis and YAP by modulating hepatocyte contractility.** (A) Representative immunofluorescence stainings for pMLC, F-actin (phalloidin) and β-galactosidase (recombined cells) in a *Capz* LKO liver section. WT indicates non-recombined hepatocytes. n = 3 mice were consistent. Scale bar = 20 μm. (B) Atomic force microscopy analyses were performed on control (WT) and *Capz* LKO livers. Left: Representative maps, with squares corresponding to single adjacent measurements. Right: Box plot (median, quartiles and extremes). n >4 maps from 2 mice of each genotype. (C) Expression of hepatocyte mechano-responsive genes as measured by RNA sequencing of whole livers from control and *Capz* LKO mice. Average expression levels in control (WT) mice were arbitrarily set equal to 1, and all other data are relative to this. n = 4 for each genotype. (D) Representative immunofluorescence stainings for pMLC on liver sections of mice of the indicated genotypes treated with or without the ROCKi, fasudil. n = 3 mice were consistent. Scale bar = 80 μm. (E) Expression of YAP target genes as measured by qPCR of whole livers from control (WT) and *Capz* LKO mice without or with fasudil (ROCKi). Gene levels relative to *GAPDH*. Average expression levels in control mice were arbitrarily set equal to 1, and all other data are relative to this. n = 4 for *Capz* LKO ± ROCKi. (F) and (G) Quantification of EdU incorporation (F) and CK19-positive atypical ductal cells (G) in livers from control (WT) and *Capz* LKO mice treated with or without fasudil (ROCKi). n = 4 for *Capz* LKO ± ROCKi. KO, knockout; LKO, liver specific KO; pMLC, phosphorylated myosin light chain; qPCR, quantitative PCR, ROCKi, ROCK inhibitor; WT, wild-type. Graphs are average and single points (mice) with unpaired 2-tailed Student's *t* test with Welch's correction. Immunostainings were repeated in independent sections of independent mice (see methods), and a representative result is shown.

assembly dynamics regulates YAP in parallel to the Hippo cascade in liver tissue.[13,52,73,74]

Capzb regulates liver homeostasis by controlling tissue mechanics

Data gathered so far indicate that *Capzb* regulates cellular forces *in vitro*, and the activity of a key mechanotransduction pathway *in vivo*. We then sought to test the idea that CAPZ also regulates tissue mechanical properties *in vivo*. For this we monitored F-actin and MLC phosphorylation[75] and found them increased in *Capz* LKO liver tissue compared to the controls (Fig. 6A). Importantly, this was associated with increased tissue stiffness, which can be an indirect readout of actomyosin contractility in cells,[76] as measured by AFM (Fig. 6B). Moreover, target genes that are inhibited in hepatocytes subjected to high stiffness[1,53] are downregulated in *Capz* LKO livers (Fig. 6C), further supporting the view that CAPZ regulates the cell's mechanical properties. To functionally validate these findings, we inhibited ROCK activity in *Capz* LKO mice, which efficiently reduced MLC phosphorylation (Fig. 6D), and scored YAP-dependent phenotypes. As shown in Fig. 6E-G, hallmark phenotypes induced by *Capzb* deletion, including expression of direct YAP target genes, were inhibited by fasudil treatment. Altogether, these data indicate a function of *Capzb* in restraining tissue tension, and a physiological role for tissue tension in regulating hepatocyte homeostasis.

Discussion

Here we found that inactivation of the capping protein *Capzb* induced increased cell tension and tissue stiffness, and enabled pMLC activity in soft environments which would normally suppress it, including the liver.[53] *Capzb* inactivation induced liver overgrowth, hepatocyte dedifferentiation and repatterning of liver metabolism, which all depend on the YAP mechanotransduction pathway. These phenotypes were similar in strength, and overlapping by gene expression analyses, with published liver mutants of the Hippo pathway, and can be readily seen by inactivating *Capzb* in adult hepatocytes. We also found that *Capzb* and Hippo inactivation cooperate to drive hepatocyte proliferation, genetically supporting the view that mechanical signals regulate YAP/TAZ through both LATS-dependent[77] and LATS-independent mechanisms.[78,79] This makes CAPZ the only genetically-validated YAP/TAZ regulator from flies[80,81] to mammals besides the Hippo pathway. We did not find evidence for a mechanical activation of β-catenin though,[82] because zonation defects are compatible, if anything, with inhibited β-catenin.[64]

Our results suggest that capping of the F-actin barbed end is crucial to regulate cell mechanics *in vitro* and *in vivo*, and a required determinant of adult liver homeostasis. The phenotypes observed in *Capzb*-null livers were stable up to 30 weeks (not shown), suggesting that the novel function that we describe here for CAPZ cannot be easily compensated, and that CAPZ plays a prominent role in regulating cell and tissue mechanotransduction. These results highlight the interesting possibility that CAPZ levels and activity are regulated in tissues, eventually contributing to pattern cell mechanics, YAP/TAZ and perhaps other mechanotransduction pathways. The existence of a whole family of CAPZ-regulatory proteins and the known, but so far poorly addressed, role of phosphoinositides as regulators of CAPZ[31] represent a possible basis to better understand how CAPZ activity, and by association F-actin assembly dynamics, are involved in the signaling mechanisms that maintain tissue homeostasis.

Conflict of interest

The authors declare no conflicts of interest that pertain to this work.

Please refer to the accompanying ICMJE disclosure forms for further details.

Authors' contributions

AP breed mice, performed experiments and analyzed data, with help from GS, PR, IB and MM; PB rederived embryos rederived mice carrying the targeted *Capzb* allele; MA designed the recombination strategy; FG and GP performed histology and pathological analyses; SB and MF performed bioinformatics analyses; ACL, AD, AP and KF performed AFM and TFM measurements; AG, AP and NG performed TIRF and FRAP experiments; AP and SD planned experiments and wrote the paper.

Supplementary data

Supplementary data to this article can be found online at https://doi.org/10.1016/j.jhep.2019.02.022.

References

Author names in bold designate shared co-first authorship

[1] Mooney D, Hansen L, Vacanti J, Langer R, Farmer S, Ingber D. Switching from differentiation to growth in hepatocytes: control by extracellular

matrix. J Cell Physiol 1992;151:497–505. https://doi.org/10.1002/jcp.1041510308.

[2] Chen CS, Mrksich M, Huang S, Whitesides GM, Ingber DE. Geometric control of cell life and death. Science (New York, NY) 1997;276:1425–1428.

[3] McBeath R, Pirone DM, Nelson CM, Bhadriraju K, Chen CS. Cell shape, cytoskeletal tension, and RhoA regulate stem cell lineage. Commitment 2004;6:483–495. https://doi.org/10.1016/S1534-5807(04)00075-9.

[4] Engler AJ, Sen S, Sweeney HL, Discher DE. Matrix elasticity directs stem cell lineage specification. Cell 2006;126:677–689. https://doi.org/10.1016/j.cell.2006.06.044.

[5] Watt FM, Jordan PW, O'Neill CH. Cell shape controls terminal differentiation of human epidermal keratinocytes. Proc Natl Acad Sci USA 1988;85:5576–5580.

[6] Weaver VM, Petersen OW, Wang F, Larabell CA, Briand P, Damsky C, et al. Reversion of the malignant phenotype of human breast cells in three-dimensional culture and in vivo by integrin blocking antibodies. J Cell Biol 1997;137:231–245.

[7] **Paszek MJ**, **Zahir N**, Johnson KR, Lakins JN, Rozenberg GI, Gefen A, et al. Tensional homeostasis and the malignant phenotype. Cancer Cell 2005;8:241–254. https://doi.org/10.1016/j.ccr.2005.08.010.

[8] Schwartz MA. Integrins and extracellular matrix in mechanotransduction. Cold Spring Harbor Perspect Biol 2010;2. https://doi.org/10.1101/cshperspect.a005066 a005066.

[9] Iskratsch T, Wolfenson H, Sheetz MP. Appreciating force and shape—the rise of mechanotransduction in cell biology. Nat Rev Mol Cell Biol 2014;15:825–833. https://doi.org/10.1038/nrm3903.

[10] Vogel V. Unraveling the mechanobiology of extracellular matrix. Annu Rev Physiol 2018;80:353–387. https://doi.org/10.1146/annurev-physiol-021317-121312.

[11] Vining KH, Mooney DJ. Mechanical forces direct stem cell behaviour in development and regeneration. Nat Rev Mol Cell Biol 2017. https://doi.org/10.1038/nrm.2017.108.

[12] Sun Z, Guo SS, Fässler R. Integrin-mediated mechanotransduction. J Cell Biol 2016;215:445–456. https://doi.org/10.1083/jcb.201609037.

[13] **Dupont S**, **Morsut L**, Aragona M, Enzo E, Giulitti S, Cordenonsi M, et al. Role of YAP/TAZ in mechanotransduction. Nature 2011;474:179–183. https://doi.org/10.1038/nature10137.

[14] Wada K-I, Itoga K, Okano T, Yonemura S, Sasaki H. Hippo pathway regulation by cell morphology and stress fibers. Development 2011;138:3907–3914. https://doi.org/10.1242/dev.070987.

[15] Dupont S. Role of YAP/TAZ in cell-matrix adhesion-mediated signalling and mechanotransduction. Exp Cell Res 2016;343:42–53. https://doi.org/10.1016/j.yexcr.2015.10.034.

[16] Piccolo S, Dupont S, Cordenonsi M. The biology of YAP/TAZ: hippo signaling and beyond. Physiol Rev 2014;94:1287–1312. https://doi.org/10.1152/physrev.00005.2014.

[17] Johnson R, Halder G. The two faces of Hippo: targeting the Hippo pathway for regenerative medicine and cancer treatment. Nat Rev Drug Discov 2014;13:63–79. https://doi.org/10.1038/nrd4161.

[18] Dong J, Feldmann G, Huang J, Wu S, Zhang N, Comerford SA, et al. Elucidation of a universal size-control mechanism in Drosophila and mammals. Cell 2007;130:1120–1133. https://doi.org/10.1016/j.cell.2007.07.019.

[19] **Camargo FD**, Gokhale S, Johnnidis JB, Fu D, Bell GW, Jaenisch R, et al. YAP increases organ size and expands undifferentiated progenitor cells. Curr Biol 2007;17:2054–2060. https://doi.org/10.1016/j.cub.2007.10.039.

[20] Yimlamai D, Christodoulou C, Galli GG, Yanger K, Pepe-Mooney B, Gurung B, et al. Hippo pathway activity influences liver cell fate. Cell 2014;157:1324–1338. https://doi.org/10.1016/j.cell.2014.03.060.

[21] **Benhamouche S**, **Curto M**, Saotome I, Gladden AB, Liu C-H, Giovannini M, et al. Nf2/Merlin controls progenitor homeostasis and tumorigenesis in the liver. Genes Dev 2010;24:1718–1730. https://doi.org/10.1101/gad.1938710.

[22] **Zhang N**, **Bai H**, David KK, Dong J, Zheng Y, Cai J, et al. Merlin/NF2 tumor suppressor functions through the YAP oncoprotein to regulate tissue homeostasis in mammals. Dev Cell 2010;19:27–38. https://doi.org/10.1016/j.devcel.2010.06.015.

[23] Lu L, Li Y, Kim SM, Bossuyt W, Liu P, Qiu Q, et al. Hippo signaling is a potent in vivo growth and tumor suppressor pathway in the mammalian liver. Proc Natl Acad Sci USA 2010;107:1437–1442. https://doi.org/10.1073/pnas.0911427107.

[24] Zhou D, Conrad C, Xia F, Park J-S, Payer B, Yin Y, et al. Mst1 and Mst2 maintain hepatocyte quiescence and suppress hepatocellular carcinoma development through inactivation of the YAP oncogene. Cancer Cell 2009;16:425–438. https://doi.org/10.1016/j.ccr.2009.09.026.

[25] **Lee K-P**, **Lee J-H**, Kim T-S, Kim T-H, Park H-D, Byun J-S, et al. The Hippo-Salvador pathway restrains hepatic oval cell proliferation, liver size, and liver tumorigenesis. Proc Natl Acad Sci USA 2010;107:8248–8253. https://doi.org/10.1073/pnas.0912203107.

[26] Lee D-H, Park JO, Kim T-S, Kim SK, Kim T-H, Kim M-C, et al. LATS-YAP/TAZ controls lineage specification by regulating TGFβ signaling and Hnf4α expression during liver development. Nat Comms 2016;7:11961. https://doi.org/10.1038/ncomms11961.

[27] Nishio M, Sugimachi K, Goto H, Wang J, Morikawa T, Miyachi Y, et al. and TGF-β signaling mediate hepatocarcinogenesis in Mob1a/1b-deficient mice. Proc Natl Acad Sci USA 2016;113:E71–E80. https://doi.org/10.1073/pnas.1517188113.

[28] Fitamant J, Kottakis F, Benhamouche S, Tian HS, Chuvin N, Parachoniak CA, et al. YAP inhibition restores hepatocyte differentiation in advanced HCC, leading to tumor regression. Cell Rep 2015;10:1692–1707. https://doi.org/10.1016/j.celrep.2015.02.027.

[29] **Hu Y**, **Shin DJ**, Pan H, Lin Z, Dreyfuss JM, Camargo FD, et al. YAP suppresses gluconeogenic gene expression through PGC1α. Hepatology 2017;66:2029–2041. https://doi.org/10.1002/hep.29373.

[30] Roca-Cusachs P, Conte V, Trepat X. Quantifying forces in cell biology. Nat Cell Biol 2017;19:742–751. https://doi.org/10.1038/ncb3564.

[31] Edwards M, Zwolak A, Schafer DA, Sept D, Dominguez R, Cooper JA. Capping protein regulators fine-tune actin assembly dynamics. Nat Rev Mol Cell Biol 2014;15:677–689. https://doi.org/10.1038/nrm3869.

[32] Guo X, Zhao Y, Yan H, Yang Y, Shen S, Dai X, et al. Single tumor-initiating cells evade immune clearance by recruiting type II macrophages. Genes Dev 2014;31:247–259. https://doi.org/10.1101/gad.294348.116.

[33] Santinon G, Brian I, Pocaterra A, Romani P, Franzolin E, Rampazzo C, et al. dNTP metabolism links mechanical cues and YAP/TAZ to cell growth and oncogene-induced senescence. EMBO J 2018;37. https://doi.org/10.15252/embj.201797780 e97780.

[34] Dobin A, Davis CA, Schlesinger F, Drenkow J, Zaleski C, Jha S, et al. STAR: ultrafast universal RNA-seq aligner. Bioinformatics 2013;29:15–21. https://doi.org/10.1093/bioinformatics/bts635.

[35] Liao Y, Smyth GK, Shi W. featureCounts: an efficient general purpose program for assigning sequence reads to genomic features. Bioinformatics 2014;30:923–930. https://doi.org/10.1093/bioinformatics/btt656.

[36] **Robinson MD**, **McCarthy DJ**, Smyth GK. edgeR: a Bioconductor package for differential expression analysis of digital gene expression data. Bioinformatics 2010;26:139–140. https://doi.org/10.1093/bioinformatics/btp616.

[37] Wang J, Shaner N, Mittal B, Zhou Q, Chen J, Sanger JM, et al. Dynamics of Z-band based proteins in developing skeletal muscle cells. Cell Motil Cytoskeleton 2005;61:34–48. https://doi.org/10.1002/cm.20063.

[38] **Bollmann L**, **Koser DE**, Shahapure R, Gautier HOB, Holzapfel GA, Scarcelli G, et al. Microglia mechanics: immune activation alters traction forces and durotaxis. Front Cell Neurosci 2015;9:363. https://doi.org/10.3389/fncel.2015.00363.

[39] Han SJ, Oak Y, Groisman A, Danuser G. Traction microscopy to identify force modulation in subresolution adhesions. Nat Methods 2015;12:653–656. https://doi.org/10.1038/nmeth.3430.

[40] Christ AF, Franze K, Gautier H, Moshayedi P, Fawcett J, Franklin RJM, et al. Mechanical difference between white and gray matter in the rat cerebellum measured by scanning force microscopy. J Biomech 2010;43:2986–2992. https://doi.org/10.1016/j.jbiomech.2010.07.002.

[41] **Avenarius MR**, **Krey JF**, Dumont RA, Morgan CP, Benson CB, Vijayakumar S, et al. Heterodimeric capping protein is required for stereocilia length and width regulation. J Cell Biol 2017. https://doi.org/10.1083/jcb.201704171.

[42] **Fu J**, **Wang Y-K**, Yang MT, Desai RA, Yu X, Liu Z, et al. Mechanical regulation of cell function with geometrically modulated elastomeric substrates. Nat Methods 2010;7:733–736. https://doi.org/10.1038/nmeth.1487.

[43] Chang C-W, Kumar S. Differential contributions of nonmuscle myosin II isoforms and functional domains to stress fiber mechanics. Sci Rep 2015;5:13736. https://doi.org/10.1038/srep13736.

[44] Murthy K, Wadsworth P. Myosin-II-dependent localization and dynamics of F-Actin during cytokinesis. Curr Biol 2005;15:724–731. https://doi.org/10.1016/j.cub.2005.02.055.

[45] **Dumbauld DW**, **Michael KE**, Hanks SK, García AJ. Focal adhesion kinase-dependent regulation of adhesive forces involves vinculin recruitment to focal adhesions. Biol Cell 2010;102:203–213. https://doi.org/10.1042/BC20090104.

[46] Zhou DW, Lee TT, Weng S, Fu J, García AJ. Effects of substrate stiffness and actomyosin contractility on coupling between force transmission and vinculin-paxillin recruitment at single focal adhesions. Mol Biol Cell 2017;28:1901–1911. https://doi.org/10.1091/mbc.E17-02-0116.

[47] Omachi T, Ichikawa T, Kimura Y, Ueda K, Kioka N. Vinculin association with actin cytoskeleton is necessary for stiffness-dependent regulation of vinculin behavior. PLoS One 2017;12. https://doi.org/10.1371/journal.pone.0175324 e0175324.

[48] Pasapera AM, Schneider IC, Rericha E, Schlaepfer DD, Waterman CM. Myosin II activity regulates vinculin recruitment to focal adhesions through FAK-mediated paxillin phosphorylation. J Cell Biol 2010;188:877–890. https://doi.org/10.1083/jcb.200906012.

[49] **Shiu J-Y**, **Aires L**, Lin Z, Vogel V. Nanopillar force measurements reveal actin-cap-mediated YAP mechanotransduction. Nat Cell Biol 2018. https://doi.org/10.1038/s41556-017-0030-y.

[50] Théry M, Racine V, Piel M, Pépin A, Dimitrov A, Chen Y, et al. Anisotropy of cell adhesive microenvironment governs cell internal organization and orientation of polarity. Proc Natl Acad SciUSA 2006;103:19771–19776. https://doi.org/10.1073/pnas.0609267103.

[51] **Schiller HB**, **Hermann M-R**, Polleux J, Vignaud T, Zanivan S, Friedel CC, et al. β1- and αv-class integrins cooperate to regulate myosin II during rigidity sensing of fibronectin-based microenvironments. Nat Cell Biol 2013;15:625–636. https://doi.org/10.1038/ncb2747.

[52] Aragona M, Panciera T, Manfrin A, Giulitti S, Michielin F, Elvassore N, et al. A mechanical checkpoint controls multicellular growth through YAP/TAZ regulation by actin-processing factors. Cell 2013;154:1047–1059. https://doi.org/10.1016/j.cell.2013.07.042.

[53] **Desai SS**, **Tung JC**, Zhou VX, Grenert JP, Malato Y, Rezvani M, et al. Physiological ranges of matrix rigidity modulate primary mouse hepatocyte function in part through hepatocyte nuclear factor 4 alpha. Hepatology 2016;64:261–275. https://doi.org/10.1002/hep.28450.

[54] Moya IM, Halder G. The Hippo pathway in cellular reprogramming and regeneration of different organs. Curr Opin Cell Biol 2016;43:62–68. https://doi.org/10.1016/j.ceb.2016.08.004.

[55] Patel SH, Camargo FD, Yimlamai D. Hippo signaling in the liver regulates organ size, cell fate, and carcinogenesis. Gastroenterology 2017;152:533–545. https://doi.org/10.1053/j.gastro.2016.10.047.

[56] Yu F-X, Meng Z, Plouffe SW, Guan K-L. Hippo pathway regulation of gastrointestinal tissues. Annu Rev Physiol 2015;77:201–227. https://doi.org/10.1146/annurev-physiol-021014-071733.

[57] Lee J-H, Kim T-S, Yang T-H, Koo B-K, Oh S-P, Lee K-P, et al. A crucial role of WW45 in developing epithelial tissues in the mouse. EMBO J 2008;27:1231–1242. https://doi.org/10.1038/emboj.2008.63.

[58] **Croci O**, **De Fazio S**, **Biagioni F**, **Donato E**, Caganova M, Curti L, et al. Transcriptional integration of mitogenic and mechanical signals by Myc and YAP. Genes Dev 2017;31:2017–2022. https://doi.org/10.1101/gad.301184.117.

[59] Zanconato F, Forcato M, Battilana G, Azzolin L, Quaranta E, Bodega B, et al. Genome-wide association between YAP/TAZ/TEAD and AP-1 at enhancers drives oncogenic growth. Nat Cell Biol 2015;17:1218–1227. https://doi.org/10.1038/ncb3216.

[60] Jezowska B, Fernández BG, Amândio AR, Duarte P, Mendes C, Brás-Pereira C, et al. A dual function of Drosophila capping protein on DE-cadherin maintains epithelial integrity and prevents JNK-mediated apoptosis. Dev Biol 2011;360:143–159. https://doi.org/10.1016/j.ydbio.2011.09.016.

[61] Tarlow BD, Pelz C, Naugler WE, Wakefield L, Wilson EM, Finegold MJ, et al. Bipotential adult liver progenitors are derived from chronically injured mature hepatocytes. Cell Stem Cell 2014;15:605–618. https://doi.org/10.1016/j.stem.2014.09.008.

[62] **Yanger K**, **Zong Y**, Maggs LR, Shapira SN, Maddipati R, Aiello NM, et al. Robust cellular reprogramming occurs spontaneously during liver regeneration. Genes Dev 2013. https://doi.org/10.1101/gad.207803.112.

[63] Chen X, Calvisi DF. Hydrodynamic transfection for generation of novel mouse models for liver cancer research. Am J Pathol 2014;184:912–923. https://doi.org/10.1016/j.ajpath.2013.12.002.

[64] Benhamouche S, Decaens T, Godard C, Chambrey R, Rickman DS, Moinard C, et al. Apc Tumor Suppressor Gene Is the "Zonation-Keeper" of Mouse Liver. Dev Cell 2006;10:759–770. https://doi.org/10.1016/j.devcel.2006.03.015.

[65] **Gougelet A**, **Torre C**, Veber P, Sartor C, Bachelot L, Denechaud P-D, et al. T-cell factor 4 and β-catenin chromatin occupancies pattern zonal liver metabolism in mice. Hepatology 2014;59:2344–2357. https://doi.org/10.1002/hep.26924.

[66] Gebhardt R, Matz-Soja M. Liver zonation: novel aspects of its regulation and its impact on homeostasis. World J Gastroenterol 2014;20:8491–8504. https://doi.org/10.3748/wjg.v20.i26.8491.

[67] **Planas-Paz L**, **Orsini V**, Boulter L, Calabrese D, Pikiolek M, Nigsch F, et al. The RSPO–LGR4/5–ZNRF3/RNF43 module controls liver zonation and size. Nat Cell Biol 2016;18:467–479. https://doi.org/10.1038/ncb3337.

[68] Gonzalez FJ, Kimura S. Understanding the role of xenobiotic-metabolism in chemical carcinogenesis using gene knockout mice. Mutat Res 2001;477:79–87.

[69] Lu L, Finegold MJ, Johnson RL. Hippo pathway coactivators YAP and Taz are required to coordinate mammalian liver regeneration. Exp Mol Med 2018;50. https://doi.org/10.1038/emm.2017.205 e423.

[70] Yi J, Lu L, Yanger K, Wang W, Hwa Sohn B, Stanger BZ, et al. LATS1 and LATS2 regulate mouse liver progenitor cell proliferation and maturation through antagonism of the coactivators YAP and TAZ. Hepatology 2016. https://doi.org/10.1002/hep.28768.

[71] Aylon Y, Gershoni A, Rotkopf R, Biton IE, Porat Z, Koh AP, et al. The LATS2 tumor suppressor inhibits SREBP and suppresses hepatic cholesterol accumulation. Genes Dev 2016. https://doi.org/10.1101/gad.274167.115.

[72] **St John MA**, **Tao W**, Fei X, Fukumoto R, Carcangiu ML, Brownstein DG, et al. Mice deficient of Lats1 develop soft-tissue sarcomas, ovarian tumours and pituitary dysfunction. Nat Genet 1999;21:182–186. https://doi.org/10.1038/5965.

[73] **Sorrentino G**, **Ruggeri N**, Specchia V, Cordenonsi M, Mano M, Dupont S, et al. Metabolic control of YAP and TAZ by the mevalonate pathway. Nat Cell Biol 2014;16:357–366. https://doi.org/10.1038/ncb2936.

[74] Feng X, Degese MS, Iglesias-Bartolome R, Vaqué JP, Molinolo AA, Rodrigues M, et al. Hippo-independent activation of YAP by the GNAQ uveal melanoma oncogene through a trio-regulated rho GTPase signaling circuitry. Cancer Cell 2014;25:831–845. https://doi.org/10.1016/j.ccr.2014.04.016.

[75] Acton SE, Farrugia AJ, Astarita JL, Mourão-Sá D, Jenkins RP, Nye E, et al. Dendritic cells control fibroblastic reticular network tension and lymph node expansion. Nature 2014;514:498–502. https://doi.org/10.1038/nature13814.

[76] Haase K, Pelling AE. Investigating cell mechanics with atomic force microscopy. J R Soc Interface 2015;12:20140970. https://doi.org/10.1098/rsif.2014.0970.

[77] Meng Z, Qiu Y, Lin KC, Kumar A, Placone JK, Fang C, et al. RAP2 mediates mechanoresponses of the Hippo pathway. Nature 2018;560:655–660. https://doi.org/10.1038/s41586-018-0444-0.

[78] Elosegui-Artola A, Andreu I, Beedle AEM, Lezamiz A, Uroz M, Kosmalska AJ, et al. Force triggers YAP nuclear entry by regulating transport across nuclear pores. Cell 2017;171. https://doi.org/10.1016/j.cell.2017.10.008 1397–1410.e14.

[79] **Chang L**, **Azzolin L**, **Di Biagio D**, Zanconato F, Battilana G, Lucon Xiccato R, et al. The SWI/SNF complex is a mechanoregulated inhibitor of YAP and TAZ. Nature 2018;563:265–269. https://doi.org/10.1038/s41586-018-0658-1.

[80] Fernández BG, Gaspar P, Brás-Pereira C, Jezowska B, Rebelo SR, Janody F. Actin-capping protein and the hippo pathway regulate F-actin and tissue growth in Drosophila. Development 2011;138:2337–2346. https://doi.org/10.1242/dev.063545.

[81] **Sansores-Garcia L**, **Bossuyt W**, Wada K-I, Yonemura S, Tao C, Sasaki H, et al. Modulating F-actin organization induces organ growth by affecting the Hippo pathway. EMBO J 2011;30:2325–2335. https://doi.org/10.1038/emboj.2011.157.

[82] Benham-Pyle BW, Pruitt BL, Nelson WJ. Mechanical strain induces E-cadherin-dependent YAP and -catenin activation to drive cell cycle entry. Science (New York, NY) 2015;348:1024–1027. https://doi.org/10.1126/science.aaa4559.

[83] Moroishi T, Hayashi T, Pan W-W, Fujita Y, Holt MV, Qin J, et al. The hippo pathway kinases LATS1/2 suppress cancer immunity. Cell 2016;167. https://doi.org/10.1016/j.cell.2016.11.005 1525–1539.e17.